

Catalytic Nanosheets

Enhanced Catalytic Activity in Liquid-Exfoliated FeOCl Nanosheets as a Fenton-Like Catalyst

Jian Zhang,^[a] Xiu-Ling Jiao,^[a, b] Yu-Guo Xia,^{*,[b]} Fang-Fang Liu,^[a] Ying-Ping Pang,^[a] Xin-Fu Zhao,^[a] and Dai-Rong Chen^{*,[a, b]}

Abstract: A facile liquid-phase exfoliation method to prepare few-layer FeOCl nanosheets in acetonitrile by ultrasonication is reported. The detailed exfoliation mechanism and generated products were investigated by combining first-principle calculations and experimental approaches. The similar cleavage energies of FeOCl (340 mJm^{-2}) and graphite (320 mJm^{-2}) confirm the experimental exfoliation feasibility. As a Fenton reagent, FeOCl nanosheets showed outstanding properties in the catalytic degradation of phenol in water at room temperature, under neutral pH conditions, and with

sunlight irradiation. Apart from the increased surface area of the nanosheets, the surface state change of the nanosheets also plays a key role in improving the catalytic performance. The changes of charge density, density of states (DOS), and valence state of Fe atoms in the exfoliated FeOCl nanosheets versus plates illustrated that surface atomistic relationships made the few-layer nanosheets higher activity, indicating the exfoliation process of the FeOCl nanosheets also brought about surface state changes.

Introduction

To meet the scientific challenges of the increasing global demand for materials with exotic properties, ultrathin 2D nanosheets of layered materials have been widely exploited in recent years.^[1] These have strong in-plane chemical bonds but weak out-of-plane van der Waals bonds between the layered materials.^[2] Owing to their advantages such as improved electrochemical and mechanical properties, ultrathin 2D nanosheets represent a promising and appealing material for high performance sensors, electronic devices, energy devices, and catalysis.^[3–6] Studies have been focused on synthesis methods for ultrathin 2D nanostructures of layered materials, such as mechanical exfoliation, liquid exfoliation, ion intercalation and exfoliation, chemical vapor deposition (CVD), and wet-chemical synthesis.^[7–11] Among these much-employed methods, liquid exfoliation has been widely used to produce single-layer or few-layer ultrathin 2D nanosheets because it is easier and more convenient than other methods.^[8] Furthermore, the as-obtained 2D nanosheets can form colloidal dispersions in solvents.^[8,9]

Nowadays, the health of humans is being seriously undermined by organic pollution caused by various production methods. The development of rapid and complete degradation of organic pollutants without causing secondary pollution is crucial for water treatment.^[12] To date, Fenton reactions, as an advanced oxidation technology, have drawn significant attention. These reactions are based on the generation of OH[•] to decompose organic molecules into small nontoxic molecules, such as CO₂, H₂O, and inorganic salts.^[13] Fenton reactions are inexpensive, safe, and environmentally friendly. Despite a series of Fenton compounds (FeOOH, Fe₂O₃, FeS), few-layer MoS₂ nanosheets, Fe₂O₃/graphene, graphite oxide (GO)-Fe₃O₄, and β-FeOOH-TiO₂ being applied to the heterogeneous reaction,^[14–20] these Fenton agents either cause secondary pollution in the treatment procedure or need rigorous conditions such as acidic medium, ultraviolet light, or high temperature, which greatly limits their practical applications.^[20–22] FeOCl, as an oxyhalide compound, possesses orthorhombic system with a layered structure, in which the adjacent layers are bonded across interlayer atoms by van der Waals interactions.^[23] FeOCl is often used as the host material of intercalation compounds because of the weak interaction between the layers.^[24,25] As a good catalyst for Fenton reactions, FeOCl shows very good performance in the catalytic degradation of aqueous organic pollutants.^[26,27] Up to now, only FeOCl plates have been prepared by solid-phase or vapor-deposition synthesis methods;^[26–28] as far as we are aware, the preparation of ultrathin FeOCl nanosheets by the easier and more convenient liquid-exfoliation method has not been reported yet.

The physical and chemical performances of exfoliated nanosheets highly depend on the preparation method because of the surface atomistic changes, adsorbed molecules, and in-

[a] J. Zhang, Prof. X.-L. Jiao, F.-F. Liu, Y.-P. Pang, X.-F. Zhao, Prof. D.-R. Chen
School of Chemistry and Chemical Engineering
Shandong University
Jinan 250100 (P. R. China)

[b] Prof. X.-L. Jiao, Dr. Y.-G. Xia, Prof. D.-R. Chen
National Engineering Research Center for Colloidal Materials
Shandong University
Jinan 250100 (P. R. China)
E-mail: jiaoxl@sdu.edu.cn
cdr@sdu.edu.cn

Supporting information for this article can be found under
<http://dx.doi.org/10.1002/chem.201600172>.

duced defects in the nanosheets.^[29,30] Therefore, knowledge of the exfoliation process and the structural characteristic of the as-exfoliated nanosheets helps shed light on the controlled synthesis of nanosheets of high quality and studying the unique properties associated with exfoliation. The cleavage energy and intercalation energy, which are the crucial criteria to judge the exfoliation difficulty of layered materials, are rarely acquired in experiments.^[31] First-principle calculations as an important supplementary means has been successfully applied to investigate the exfoliation of MnPSe₃, the exfoliation and intercalation process of graphite by Brønsted acids, single layers of K₂CuF₄ and Ca₂N nanosheets, etc.^[31,34] Unfortunately, the exfoliation and intercalation mechanism of FeOCl has not been studied, and the catalytic mechanism of H₂O₂ decomposition on the FeOCl surface to yield hydroxyl radical is not clear either.

Herein, we have used a facile liquid-phase exfoliation method to prepare few-layer FeOCl nanosheets. The detailed exfoliation mechanism and generated products were investigated by a combined first-principle calculation and experimental approach. We arrived at FeOCl nanosheets by first studying the cleavage energy. As a Fenton reagent, FeOCl nanosheets show superior performance in the catalytic degradation of phenol in water compared with plates at room temperature, under neutral pH conditions, and with sunlight irradiation. To evaluate the catalytic performance of exfoliated few-layer FeOCl nanosheets, contrast experiments were done to investigate whether the enhanced catalytic activity was only caused by the surface area effect. We further studied the charge density and density of state changes of the exfoliated FeOCl nanosheets versus plates, illustrating that the surface atomistic relationship also made the few-layer nanosheets more active owing to the decrease in band gap in the visible-light region. Moreover, the valence of Fe^{III} decreased with decreasing thickness. All the evidence regarding the nanosheets clearly indicates that the exfoliation process of FeOCl plates brings about surface state changes, which promotes generation of OH[•] radicals and phenol degradation.

Results and Discussion

Chemical intrinsic exfoliation mechanism and the as-prepared few-layer FeOCl nanosheets

In liquid exfoliation, the cleavage energy and solvent surface tension are introduced to judge the exfoliation feasibility. For the purpose of studying the exfoliation possibility of FeOCl, we first calculated the cleavage energy, which is 340 mJ m⁻² (Figure S3a in the Supporting Information). Additionally, the cleavage energy of graphite was also calculated for exfoliation criterion,^[31–34] and the calculated value of 320 mJ m⁻² (Figure S3b) is very close to the experimentally estimated one (360 mJ m⁻²).^[35] Clearly, the similar cleavage energies of FeOCl and graphite imply that the exfoliation of bulk FeOCl is feasible experimentally. Apart from the cleavage energy, the surface tension of the solvent should be matched with the surface energy of the 2D nanosheets.^[36] The small difference between

surface energy of FeOCl (80 mJ m⁻²) and graphite (120 mJ m⁻²) in our calculations confirms the realistic possibility for exfoliation in liquid. In experiment, the surface tension needed for the exfoliation of graphite is about 40–50 mJ m⁻².^[37,38] Based on the various organic solvents containing -CN groups that have been intercalated in FeOCl interlayers and the easy intercalation associated with small carbon chain length,^[24,25,39] acetonitrile (29.58 mJ m⁻²) was chosen as the solvent. To further confirm the energetically favorable rationality of acetonitrile, we then calculated the adsorption and optimized structures of -CN or -CH₃ on the FeOCl (010) crystal face and interlayer (Figure S4 in the Supporting Information). The larger adsorption energy of the -CN group (-0.22 eV, Figure S4a) than that of the -CH₃ group (-0.16 eV, Figure S4b) indicates the stronger adsorption of -CN on the FeOCl surface than -CH₃. Furthermore, the negative intercalation energy (-0.39 eV) in Figure S4c implies an energetically favorable intercalated stage. Otherwise, the distances of N...Cl and H...Cl reveal the electrostatic attraction between CH₃CN and the FeOCl surface (Figure S4a–c). In addition, acetonitrile and water can mutually dissolve each other, which removes the effect of acetonitrile on the catalysis of FeOCl in water in the next step.

Inspired by the above DFT calculations, the FeOCl nanosheets were successfully exfoliated in acetonitrile. The XRD patterns in Figure 1a show the pure phase of the FeOCl plates (orthorhombic lattice, JCPDS, No. 24-1005) and a highly preferred (010) orientation in the plates.^[40] After exfoliation, the absence of (010) peaks in the nanosheets confirms the successful exfoliation (Figure 1a).^[41] The atomic percent of Fe, O, and Cl in the nanosheets is 1:1.1:0.9 from the results of energy-dispersive X-ray spectroscopy (EDS; Figure S5a), implying the nanosheets

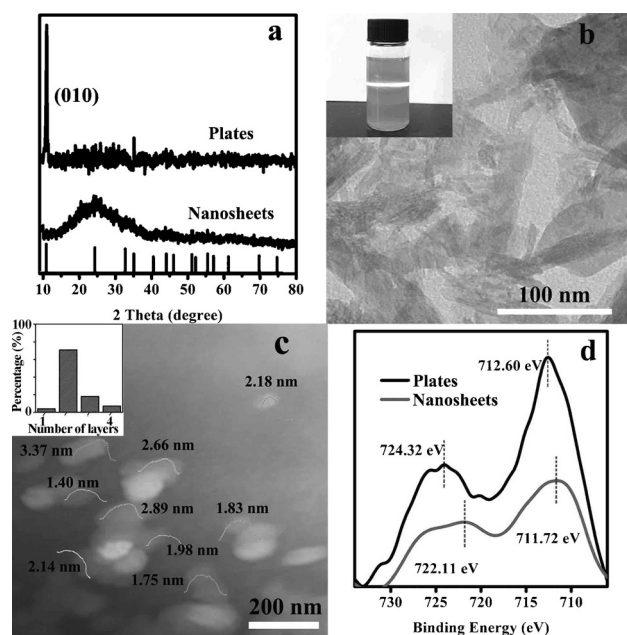


Figure 1. (a) XRD patterns of FeOCl plates and nanosheets. (b) TEM image of FeOCl nanosheets, inset: Tyndall effect of FeOCl nanosheets in acetonitrile. (c) AFM pattern of FeOCl nanosheets, inset: layer number distribution of nanosheets. (d) XPS of Fe 2p in FeOCl plates and nanosheets.

are FeOCl. TEM images indicate that the exfoliated nanosheets have faint contrast compared with FeOCl plates (Figure 1 b and Figure S5b), which is consistent with their thin nature.^[42] The Tyndall effect observed upon irradiating the solution with a laser beam confirms the colloidal nature, which also proves the successful exfoliation to nanosheets (Figure 1 b). It is worth noting that the height of solution-processed 2D nanosheets is overestimated by atomic force microscopy (AFM) measurements because of molecule adsorption on the exfoliated flakes' surface to passivate the surface and maintain the structural stability.^[43,44] Clearly, the emergent vibration peaks of CH₃CN in the FTIR spectrum of the as-prepared nanosheets implies the existence of acetonitrile on nanosheets' surface (Figure S6 in the Supporting Information). We calculated the thickness of FeOCl as a bare surface and a coated surface with adsorbed CH₃CN (both sides) of one to four layers (Table S2). The thickness in Figure 1 c is about 1.40–3.37 nm, which corresponds to one to four layers of FeOCl. In sharp contrast, the thickness of FeOCl plates is about 140–160 nm with several micrometers width from the results of SEM and AFM (Figure S5 c and 5 d). In particular, the layer number distribution determined by analyzing 100 nanosheets discloses that bilayer FeOCl nanosheets are in the majority (see the inset in Figure 1 c). Although one to four layers of FeOCl nanosheets can be obtained simultaneously by liquid-phase exfoliation, the mean layer number is that of a bilayer structure.

To gain insights into the variation of the electronic state, X-ray photoelectron spectroscopy (XPS) analysis was performed (Figure 1 d). The lower binding energy of Fe 2p in nanosheets compared with plates indicates the reduction of the valence state Fe^{III} in the FeOCl nanosheets. To further understand the variation of the electronic state, the charge redistribution was calculated before and after exfoliation by using the Bader method (Table 1). The interaction of Fe–O and Fe–Cl in bilayer

	Fe	O	Cl
bulk	6.47	7.04	7.48
bilayer	6.76	6.91	7.33

FeOCl nanosheets decreases compared with the bulk material owing to the decreased valence electron numbers of O and Cl (7.04 for O and 7.48 for Cl in bulk, 6.91 for O and 7.33 for Cl in bilayer). Significantly, the valence electron numbers of Fe in bilayer FeOCl nanosheets increase from 6.47 to 6.76, strongly highlighting the reduction of the valence state for Fe atoms, in accord with the XPS results (Figure 1 d). Taken together, it is clear that the valence state of Fe^{III} diminished with decreasing FeOCl thickness. It is worth noting that, in Fenton reactions, the generation rate of OH[•] over Fe^{II} is proven to be higher than that over Fe^{III}.^[45] As a result, the reduction of Fe^{III} in the FeOCl nanosheets is of benefit to the electron/charge transfer to H₂O₂ and further promotes the generation of OH[•].

An additional study on surface state difference of FeOCl bulk and nanosheets was carried out by calculating their total and partial electronic density of states (TDOS and PDOS). As illustrated by the TDOS of bulk FeOCl (Figure 2 a), the band gap is 1.84 eV, which is close to our experimental (1.91 eV, Figure S7 in the Supporting Information) and literature values

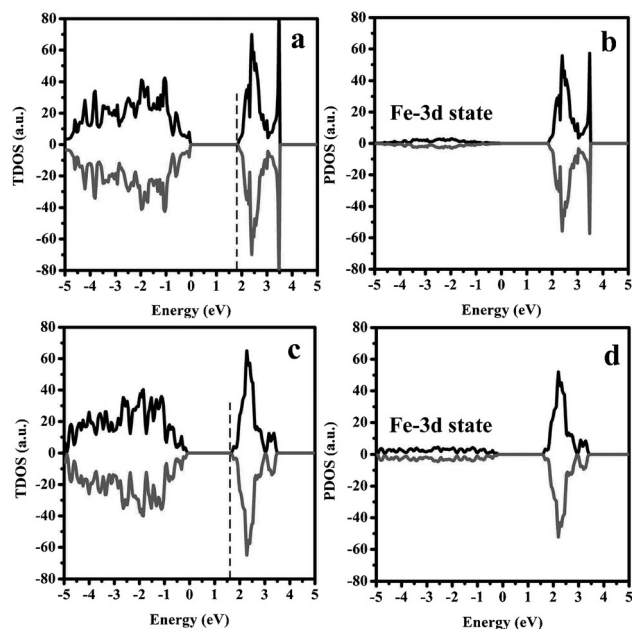


Figure 2. (a) TDOS and (b) PDOS of the bulk. (c) TDOS and (d) PDOS of the bilayer sample.

(1.90 eV).^[24] In photo-Fenton reactions, UV light is usually adopted to promote the conversion of Fe^{III} to Fe^{II} to activate the reaction.^[46] The smaller band gap of FeOCl compared with other iron oxides (Fe₂O₃ or FeOOH) can effectively increase the sunlight utilization.^[14,15] The calculated band gap in the bilayers decreases to 1.70 eV (Figure 2 c) and it is 1.82 eV in our experiment (Figure S7). The reduced band gap is conducive to electronic transitions and transmission. The contribution to the conduction band minimum (CBM) arises from the Fe3d orbital whereas the valence band maximum (VBM) potentials come from the contribution of Cl and O2p orbitals (Figure 2 b and 2 d).

Enhanced catalytic activity of exfoliated FeOCl nanosheets as Fenton-like catalysts

In the Fenton reaction it is highly challenging to achieve high catalysis in neutral solution because the iron compounds easily react with acid, causing iron leaching. Therefore, to avoid iron leaching, a neutral solution was adopted in our experiment. The phenol degradation over FeOCl plates and nanosheets (called **2L**) with the same weight (SW) and surface area (SSA) was studied (Figure 3 a). In 10 min, the phenol degrades completely over **2L** whereas it only partly degrades (54.4%) over **Plates-SW**. Furthermore, only about 3 min is needed to reach 50% degradation over **2L** whereas it takes 10 min over **Plates-**

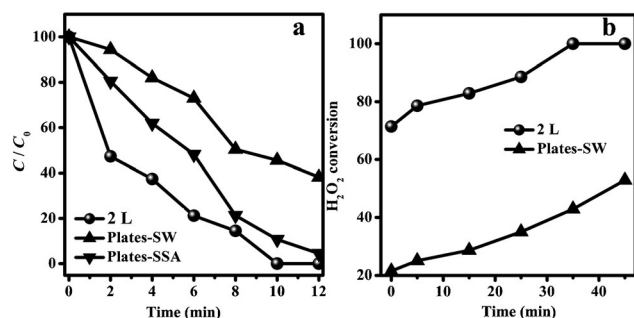


Figure 3. (a) Phenol degradation and (b) generation of OH^\bullet radicals over FeOCl nanosheets and plates at various reaction times. **2L** represents the FeOCl nanosheets owing to mainly bilayer materials being present in the sample (Figure 4c). **Plates-SW** and **Plates-SSA** are abbreviations for FeOCl plates with the same weight or same surface area compared to the exfoliated nanosheets, respectively.

SW. The catalytic performance of **2L** is clearly better than that of **Plates-SW**. It is well established that the degradation of phenol by using Fenton reactions first leads to intermediates forming, including catechol, hydroquinone, and benzoquinone, which can further react with OH^\bullet radicals to form carboxylic acids (such as oxalic and formic acid) and eventually mineralize to CO_2 and H_2O .^[47–49] There is still residual formic acid in the solution after degradation over **2L** for 10 min, as measured by HPLC-MS. The recycling performance of the FeOCl nanosheets was measured by recovering the solid catalyst through high-speed centrifugation (13000 rpm) and they were reused in the following cycle after washed with ultrapure water. After four cycles, the FeOCl nanosheets can still reach 90% degradation in 10 min (Figure S8 in the Supporting Information). The leaching amount of Fe ions was also measured, which is 1.02 ppm in first cycle and 1.98 ppm in fourth cycle, meeting the content standards for iron in water in the EU and US (<2 ppm).^[27]

According to Brunauer–Emmett–Teller (BET) measurements, the surface areas of the plates and **2L** are $2.60\text{ m}^2\text{ g}^{-1}$ and $54.17\text{ m}^2\text{ g}^{-1}$, respectively (Figure S9a–b). Notably, the degradation efficiency of **Plates-SSA** compared with **Plates-SW** increased. Although the degradation efficiency is improved, the phenol degradation is still not complete in 10 min over FeOCl **Plates-SSA** (Figure 3a). The generation of OH^\bullet radicals with super oxidation is crucial for degradation in the Fenton reaction. By using terephthalic acid as a trapping agent, we further measured the generation of OH^\bullet radicals as the active group for phenol degradation. As shown in Figure 3b, in the first few seconds after adding H_2O_2 , the generation of OH^\bullet radicals reaches 70% in the **2L** system whereas only 21% generation is seen in the **Plates-SW** system. After 35 min, the H_2O_2 conversion reaches 100% in the **2L** system and 45% in the **Plates-SW** system. The higher generation rate of OH^\bullet radicals in the **2L** system is mainly caused by the larger surface area of **2L** when **2L** and the plates have the same weight, which is also consistent with the higher degradation efficiency of **2L** in Figure 3a. Thus, together, the results from Figure 3a and b clearly show that the surface area plays a significant role,^[50,51] but is not the only reason that contributes to the improved catalytic performance.

To further study the effect of surface area on the generation of OH^\bullet radicals, we also prepared nanosheets with different thicknesses (Figure S10 in the Supporting Information). The mean thicknesses of **Sample-1**, **Sample-2**, and **Sample-3** are about 20, 10, and 5.88 nm (about 6–7 layers), respectively (Figure S10a–c). The corresponding BET surface areas of **Sample-1**, **Sample-2**, and **Sample-3** are 28.27, 35.13, and $49.47\text{ m}^2\text{ g}^{-1}$ (Figure 4a and Figure S10d–f). In addition, the surface area increases following thickness reduction (Figure 4a). We further

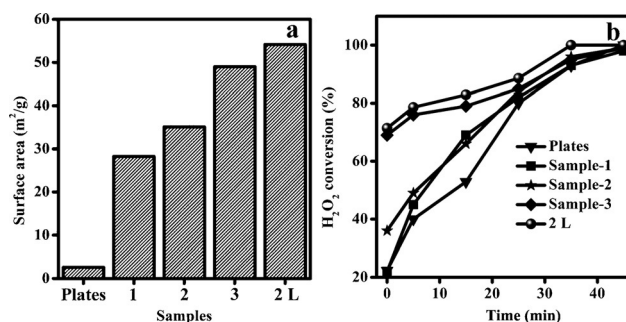


Figure 4. (a) Surface areas of the FeOCl plates, **Sample-1**, **Sample-2**, **Sample-3**, and **2L**. (b) Generation of OH^\bullet radicals over FeOCl with different thicknesses.

measured the generation of OH^\bullet radicals over FeOCl with different thicknesses but with the same total surface area (Figure 4b). The performances of OH^\bullet radical generation over **Sample-1** and **Sample-2** are slightly better than that over plates, however, there is a clear increase with **Sample-2** and **2L**. This clearly indicates that the generation of OH^\bullet radicals increases following the thickness decrease, and increases significantly when the nanosheets thickness is less than 10 nm. Clearly, the performance of OH^\bullet radical generation over **2L** is the best. These results also clearly point towards the fact that the increased surface area in FeOCl nanosheets is not the only reason for the improved performance.

Evolutional mechanism of H_2O_2 on the surfaces of the few-layer FeOCl nanosheets

Together with the results from XPS and valence electron populations (Figure 1 and Table 1), the valence state of Fe^{III} in the nanosheets decreases with decreasing thickness, which is beneficial for electron/charge transfer and the generation of OH^\bullet radicals. In addition, the decreased band gap of the nanosheets also increases sunlight utilization (Figure 2 and Figure S7). Although the comparison between monolayers and four-layer samples cannot completely reflect the actual situation, it gives some idea about the thickness-dependence of the surface state change. Hence, we further calculated the surface state change in one- and four-layered nanosheets.

Based on the consideration that Cl atoms in the surface may be lost in water owing to the weak interaction between Fe–Cl,^[27] two types of surface terminations (Fe–O atom termination (OAT) and Cl atom termination (CAT)) are considered in

our calculations (Figure S11 in the Supporting Information), which is consistent with metal oxychloride homologues in solution.^[52] The loss of Cl atoms from the FeOCl surface causes unsaturated Fe atom coordination, which become highly reactive sites. The charge density of four-layer FeOCl illustrates that the charge accumulates mostly at the interface between Fe and Cl atoms (Figure 5a) with decreased bond length for Fe–

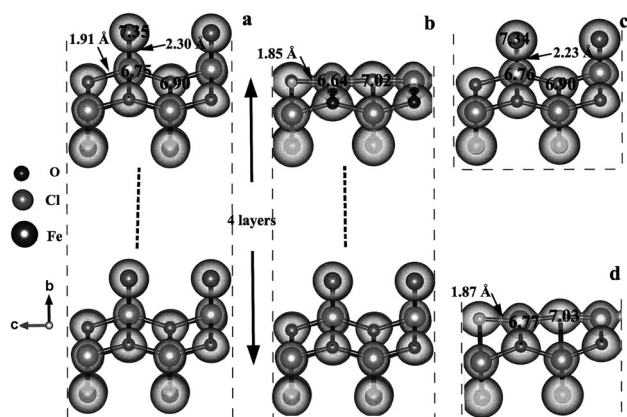


Figure 5. The charge density of (a) four-layer and (c) monolayer surfaces with CAT, and (b) four-layer and (d) monolayer surfaces with OAT. The isosurface level is 0.1 and the gray around atoms represents the charge density.

Cl (2.30 Å) compared with that of the bulk (2.35 Å). The charge density at the interface between Fe and Cl atoms in the monolayer is squeezed owing to the decreased bond length (2.23 Å, Figure 5c), indicating the increased interaction of Fe–Cl in the monolayer. The charge density at the interface between Fe and O atoms accumulates and the interaction of Fe–O also increases in monolayer nanosheets. The surface change from CAT to OAT becomes more difficult in the monolayer compared with the four-layer system. In Figure 5b,d, the clear accumulation of charge at the interface between Fe and O atoms in the surface with OAT indicates their increased interaction. In addition, the bond length of Fe–O in the four-layer surface is a little smaller than that in the monolayer (1.85 Å in four-layer surface and 1.87 Å in monolayer). The charge accumulation between Fe and O in Figure 5d decreases and is col-

lapsed compared with that in Figure 5b. In the FeOCl surface with CAT, the valence electron numbers of Fe are 6.75 in the four-layer and 6.76 in the monolayer systems, implying a reduced valence state of Fe atoms in the monolayer nanosheets. The valence electron numbers of Cl atoms are 7.34 in the monolayer and 7.35 in the four-layer system, indicating decreased electronegativity of the Cl atoms in the monolayer. In addition, the valence electron numbers of Fe atoms are 6.77 in the monolayer and 6.64 in the four-layer system with OAT, implying also the reduced valence state of Fe atoms in the monolayer nanosheets. In brief, the valence state of Fe^{III} gradually decreases with decreasing layer number, which is consistent with the XPS results (Figure 1 d).

In addition, the adsorption of molecules on active sites in the catalyst also greatly affects the catalytic activity, as the adsorption is a rate-determining process and mainly occurs on the surface of the catalytic agent.^[53] Owing to the short transmission distance of OH[•] radicals in solution, the degradation occurred on the catalytic agent's surface. To further confirm the effect of surface state change on catalysis, we also calculated the adsorption of phenol, H₂O, and H₂O₂ on the FeOCl surface, which is essential to understand the mechanism of the improved degradation performance with the nanosheets. The FeOCl plate is dominated by the (010) plane with a side face of (101).^[27] In the following, adsorption on the (010) plane is calculated first because of the small proportion of the side area in the nanosheets (about 5%).

The adsorption of phenol and H₂O₂ increase with increasing layer number (Figure 6a,b) because the additional layers also adsorb. The adsorption energy increases significantly from monolayer to bilayer nanosheets. The adsorption energy difference ($M_{\text{layer}} \geq 3$) is so small (0.03 eV for phenol and 0.05 eV for H₂O₂) that we believe further increasing the layer number has little effect on adsorption. The adsorption of H₂O, phenol, and H₂O₂ on FeOCl nanosheets with bilayers was calculated and compared (Figure 6c). Although the adsorption energies of H₂O are –0.15 eV on CAT and –0.20 eV on OAT surfaces, they are the smaller than those of phenol and H₂O₂ (Figure 6c). Two adsorption sites are considered for phenol on the FeOCl surface in our calculations; the H site and the OH site (Figure S11 a–b). The adsorption energies of the OH site and H site on the CAT surface are –0.36 eV and –0.39 eV, whereas they

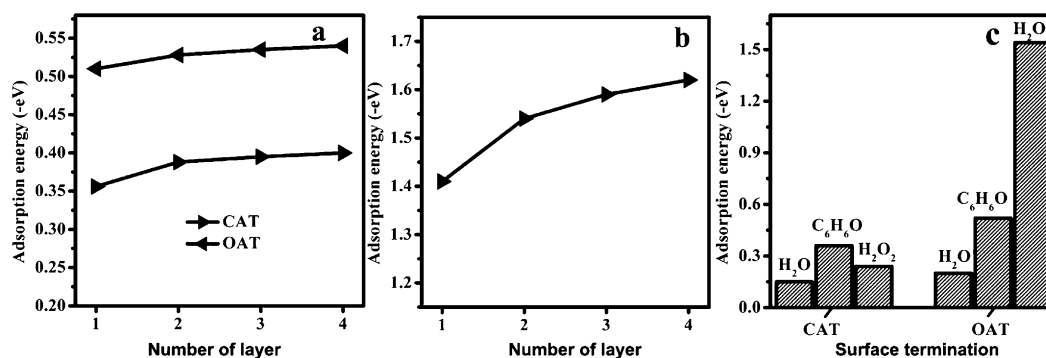


Figure 6. Adsorption energies of (a) phenol on OAT and CAT surfaces, (b) H₂O₂ on the OAT surface with one to four layers, and (c) H₂O, phenol (OH site), and H₂O₂ (G1 site) on the CAT and OAT sites of the bilayer surface.

are -0.52 eV and -0.33 eV on the OAT surface (Figure S10a–d). The adsorption energies of phenol are larger than that of H_2O_2 , indicating the energetically favorable adsorption of phenol in aqueous solution. All of the adsorptions on the FeOCl surface are based on electrostatic attraction (Figure S12 in the Supporting Information). In short, the adsorption of phenol on FeOCl nanosheets is favorable for the catalytic reaction. Additionally, the smaller adsorption energy of H_2O_2 on the CAT (-0.24 eV) than the OAT surface (-1.54 eV; Figure 6c) reveals the direct interaction between H_2O_2 and Fe atoms.

Considering the effective reaction of H_2O_2 on the FeOCl surface, H_2O_2 can be paired with Fe atoms on the G1 site (H and O in H_2O_2 point to O and Fe in the surface) of the OAT surface, and is decomposed to hydroxyl groups and OH^\cdot radicals with large adsorption energies (-1.54 eV, Figure 6c and Figure 7a).

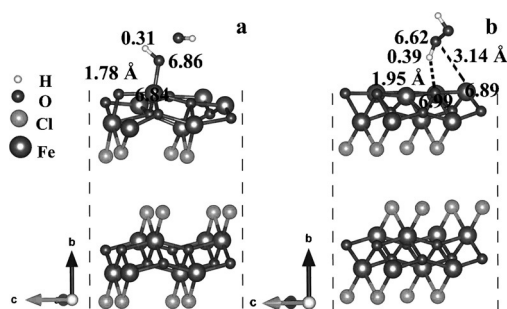


Figure 7. Optimized geometries of H_2O_2 on the FeOCl bilayer with OAT at the (a) G1 and (b) G2 adsorption sites.

Charge accumulates mostly at the interface between Fe and OH (Figure S13a in the Supporting Information). Considering another adsorption site, that of the G2 site (H in H_2O_2 points to O in the surface), the adsorption energy is just -0.52 eV and the distance between H in H_2O_2 and O in the surface is 1.95 Å (Figure 7b). There is no charge accumulation at the interface between Fe and H_2O_2 (Figure S13b). The valence electron numbers of Fe, O, and H are 6.84, 6.86, and 0.31 in G1, whereas they are 6.89, 6.99, and 0.39 in G2 (Table 2, Figure 7). The decreased valence electron number of the Fe atoms in Figure 7a compared with Figure 7b implies the transfer of electrons in Fe atoms to H_2O_2 to form OH^\cdot radicals.

Fe	O	Cl
6.84	6.86	0.31
6.89	6.99	0.39

In fact, after exfoliation, not only the thickness of the nanosheets decreases but also the size of the nanosheets decreases (Figure 1c, Figure S5b–c). This means that the ratio of the side surface area in the nanosheets increases. Therefore, we also calculated the adsorption on the side face to study the effect on catalysis. Two surface terminations (Cl–O and Fe–O termi-

nation) are considered on the (101) face (Figure S14a–b in the Supporting Information). The smaller surface energy of Fe–O termination implies the more stable surface structure (2088 mJm^{-2} for Cl–O and 1132 mJm^{-2} for Fe–O termination). The adsorption energy of phenol is -0.373 eV, implying realizable adsorption on the (101) face. Considering the decomposition of H_2O_2 caused by reaction with Fe atoms,^[27] the surface O atoms in the (101) face are not conducive to the reaction. In addition, the smaller valence electron number of Fe atoms in the (101) surface (6.70) compared with the (010) crystal face (6.76, Table 1) indicates lower catalytic activity at the (101) surface. The proportion of the side face area is about 5% in **2L**. Therefore, the increased surface area of the side face can improve the adsorption of phenol, but may have smaller contribution to the decomposition of H_2O_2 than the (010) crystal face.

To date, the mechanism of heterogeneous Fenton reactions is still unclear. The H_2O_2 decomposition and the organic compounds degradation mainly occur on the iron oxide surface.^[50] A generally accepted point for the mechanism of heterogeneous Fenton reactions consists of four parts: (1) the oxo-bridged configuration ($[\text{Fe}-\text{O}-\text{Fe}]^{\text{IV}}$),^[54] (2) the reduction of Fe^{III} ($\text{Fe}^{\text{III}} \rightarrow \text{Fe}^{\text{II}}$) on the surface,^[15] (3) the specific catalytic sites on the surface,^[55] and (4) the annihilation of OH^\cdot radicals and OH^- .^[45] As for FeOCl, the Fe atoms on the surface are in an orderly linear configuration (O–Fe–Cl or Fe–O–Fe). After exfoliation, the number of surface Fe atoms increases in the FeOCl nanosheets, which benefits the H_2O_2 decomposition. As a result of smaller adsorption energies and larger bond length of OH^- in monolayer nanosheets (-1.41 eV and 1.79 Å, Figure S15) compared with bilayer sheets, the abundance of OH^- in FeOCl nanosheets decreases. Therefore, the annihilation of OH^\cdot radicals and OH^- is inhibited, which decreases the OH^\cdot radical consumption. For the nanosheets with OAT, the bond length of Fe–O decreases to 1.85 Å from 1.91 Å. In addition, the charge density of Fe atoms on the surface is delocalized (Figure 5). The increased delocalization in the nanosheets benefits the reduction of Fe^{III} ($\text{Fe}^{\text{III}} \rightarrow \text{Fe}^{\text{II}}$) on the surface and further promotes the generation of OH^\cdot radicals.

Based on the above analysis, the adsorption of phenol on the FeOCl surface decreases the transmission distance of OH^\cdot radicals because the degradation mainly occurs on the FeOCl surface. Then, the degradation of phenol sequentially takes place in solution, when the OH^\cdot radicals diffuse to near the surface. The increased bond length of Fe–O in the monolayer with OAT indicates a decreased interaction of Fe–O, which promotes the interaction of Fe– H_2O_2 . The large adsorption energy of H_2O_2 on the FeOCl surface and the reduced valence of Fe^{III} are both propitious to the generation of OH^\cdot radicals.

Conclusion

FeOCl nanosheets were prepared by a liquid-phase exfoliation method with ultrasonic treatment in acetonitrile. The few-layer FeOCl nanosheets showed excellent catalytic performance in phenol degradation compared with plates. Apart from increased surface area after exfoliation, the surface state change

of the nanosheets also plays a great role in their catalytic properties. The increased delocalization in the nanosheets and the reduction of Fe^{III} (Fe^{III} → Fe^{II}) in the nanosheets promote the generation of OH[•] radicals. The investigation of FeOCl nanosheets provides an opportunity to gain significant fundamental insights into catalytic processes. These results may shed new light on such catalytic processes and could be extrapolated to benefit other 2D nanosheets for use as Fenton reagents.

Experimental Section

All of the chemicals were purchased from Sinopharm Chemical Reagent Co., Ltd., and were of analytical grade and used without any further purification.

Exfoliation of FeOCl plates into bilayer nanosheets

We used a solid-phase method to synthesize FeOCl plates.^[26] Exfoliation of the FeOCl plates was performed by dispersing the FeOCl plates (0.05 g) in acetonitrile (5 mL). The suspensions were treated for 30 min at ambient temperature with 250 W ultrasonication. To remove any non-exfoliated particles, the suspension was kept without disturbance for 24 h and subjected to 10 min of centrifugation at 10000 rpm. The supernatant was then centrifuged at 13000 rpm for 30 min. The final exfoliated nanosheets were obtained and then dried at 90 °C in a vacuum oven for 12 h.

Catalytic activity measurements of FeOCl plates and bilayer nanosheets

The Fenton catalytic performance of FeOCl nanosheets was tested by the degradation of phenol with H₂O₂ at pH 7 (initial pH value of phenol solution) under sunlight and at room temperature. In a typical experiment, FeOCl nanosheets (10 mg) were added to a phenol solution (100 mL, 100 mg L⁻¹) and stirred for 60 min to reach the adsorption equilibrium. The reaction was initiated by adding H₂O₂ aqueous solution (0.1 mL, 30 wt%). During the reaction, aliquots (5 mL) of the reaction mixture were taken out at certain time intervals (2 min) and centrifuged before measuring the UV/Vis absorption spectra. In addition, the Fenton reaction using FeOCl plates with the same weight (10 mg) was carried out as a comparison. The degradation of phenol was monitored by the changes in the phenol absorption peak at 270 nm in the UV/Vis spectra. To study the surface effect after exfoliation, the catalytic activity of the FeOCl plates with the same surface area compared to the nanosheets was also determined.

The production of OH[•] radicals on FeOCl plates and bilayer nanosheets

The formation of OH[•] radicals on FeOCl plates and nanosheets surface was determined by fluorescence techniques using terephthalic acid as a trapping agent, which can be reacted with OH[•] radicals to produce a highly fluorescent product (2-hydroxyterephthalic acid).^[56] The intensity of the fluorescent peak (2-hydroxyterephthalic acid) was known to be proportional to the amount of OH[•] radicals.^[57] The concentration of the terephthalic acid solution was 5 × 10⁻⁴ M in a diluted NaOH aqueous solution (2 × 10⁻³ M); it has been proved that the hydroxylation reaction of terephthalic acid proceeds mainly by OH[•] radicals under the present experimental conditions.^[58] FeOCl nanosheets (10.0 mg) were added to terephthalic acid solution (100 mL) and stirred for 30 min. Then, the reaction

was initiated by adding H₂O₂ aqueous solution (0.1 mL, 30 wt%). During the reaction, aliquots (5.0 mL) of the reaction mixture were taken out at certain time intervals (10 min) and centrifuged before measuring the fluorescence with a spectrophotometer. A peak at the wavelength of about 425 nm (2-hydroxyterephthalic acid) by excitation with the wavelength of 315 nm was achieved. The production of OH[•] radicals on FeOCl plates with the same weight and surface area compared with the nanosheets was also measured by using the above method for comparison.

Characterization

The phase structure of the product was identified by using XRD (scan rate = 2° min⁻¹; scan step = 0.06°) with a Rigaku D/Max 2200-PC diffractometer with the tube electric voltage and current of 40 kV and 35 mA for Cu_{Kα} radiation (λ = 0.15418 nm) and a graphite monochromator at ambient temperature. The shape and size of the samples were characterized by TEM (JEM-100CXII) with an accelerating voltage of 80 kV. The Fourier transform infrared (FTIR) spectra were measured with a Nicolet SDX-FTIR spectrometer by using the KBr pellet method in the range 400–4000 cm⁻¹. The Brunauer–Emmett–Teller (BET) surface area (S^{BET}) was measured by N₂ adsorption at 77 K by using a QuadraSorb SI surface area analyzer. The scanning electron microscopy (SEM) images were obtained with a Field Emission-SEM ZEISS system. Qualitative chemical analyses were performed by using energy-dispersive X-ray spectrometry (EDS) at 15 kV. The UV/Vis absorption spectra were collected with a UV/Vis spectrophotometer (Lambda-35, PerkinElmer). Atomic force microscopy (AFM, multimode 8, Bruker) was applied to measure the thickness of the FeOCl nanosheets. Fluorescence was analyzed on a Cary Eclipse fluorescence spectrophotometer. X-ray photoelectron spectra (XPS) were acquired on a PerkinElmer PHI-5300 ESCA. The binding energies obtained in the XPS analysis were corrected for specimen charging by referencing C 1s to 284.6 eV. The products of the degradation of phenol were measured by HPLC-MS (Agilent 6510). The leaching of Fe after reaction was analyzed by using an ICP-MS (Nu ATTOM).

Theoretical methods and models

To give an insight into the exfoliation process, first-principle calculations were performed with the Vienna ab initio simulation package (VASP).^[59] The exchange-correlation functional was constructed by the generalized gradient approximation (GGA)^[60] and ion–electron interactions were described by the projector-augmented wave (PAW) potential^[61] with the cutoff energy at 500 eV whereas van der Waals contributions were evaluated with the Grimme-D2 approach included for surface molecular adsorption.^[62] The Brillouin zone was sampled by a Γ -centered grid,^[63] and k -points mesh 10 × 5 × 12 for bulk and 4 × 4 × 1 for (010) and (101) surface geometry optimization calculations were used, respectively. In addition, a 2 × 2 supercell was constructed for surface molecular adsorption calculations. Both the lattice constant and the positions of all atoms were relaxed until the convergence criteria reached 1 × 10⁻⁵ eV for the total energy and 0.02 eV Å⁻¹, respectively.

As shown in Figure S1, a typical crystal structure of FeOCl has a lamellar structure. The adjacent layers are bonded in the b -direction across the chlorine atom planes by van der Waals interactions. Admittedly, iron-based composites exhibit ferromagnetic properties because of the non-half or fulfilled 3d electrons.^[64] Herein, our calculations also show that the antiferromagnetic structure of FeOCl is the most stable structure (Table S1). Therefore, all of our calculations are based on the antiferromagnetic structure. The DFT + U method was used to calculate the electronic density of states

(DOS). In the present work, the value of U was set as follows:^[65,66] 5.0 eV for the d states of Fe, 4.8 eV for the p states of O, and 7.0 eV for the p states of Cl.

In the cleavage energy calculations, a fracture in the bulk containing four layers was used, and the vacuum distance between the two fractures is more than 20 Å. The exfoliation procedure is simulated by calculating the total energy under variation of the separation, d_0 , between the fractured parts (Figure S2). Considering that the cleavage energy and interlayer interaction do not strongly depend on the number of bulk layers,^[34] the exfoliation of a FeOCl monolayer from bulk using a four-layer slab was simulated (Figure S2). The cleavage energy calculations were as follows [Eq. (1)]:

$$E_{cl} = E_{d_x} - E_{d_0} \quad (1)$$

where E_{cl} is the cleavage energy, E_{d_x} is the total energy of FeOCl when the interlayer distance is d_x , E_{d_0} is the total energy of FeOCl when the interlayer distance is d_0 .

To reveal the optimal adsorption location of H_2O_2 , phenol, and H_2O on the FeOCl nanosheet surface, DFT calculations were also performed to observe the stable geometries according to adsorption energies [Eq. (2)].

$$E_{ads} = E_{slab+adatoms} - E_{slab} - E_{adatoms} \quad (2)$$

where $E_{slab+adatoms}$ is the energy of FeOCl slab with adsorbed molecule after optimization, E_{slab} is the energy of the FeOCl slab, and $E_{adatoms}$ is the energy of the molecules.

To understand the surface state change, the electron density and the electronic density of states (DOS) were also calculated. The Bader electron population was also calculated to study the interaction between the adsorbed molecules and FeOCl surface.

Acknowledgments

This work is supported by the National Natural Science Foundation of China (Grant 21271118) and the Taishan Scholars Climbing Program of Shandong Province (tspd20150201).

Keywords: 2D nanosheets • adsorption • catalysts • density functional calculations • FeOCl

- [1] F. Xia, H. Wang, D. Xiao, M. Dubey, A. Ramasubramaniam, *Nat. Photon.* **2014**, *8*, 899–907.
- [2] A. Gupta, T. Sakthivel, S. Seal, *Prog. Mater. Sci.* **2015**, *73*, 44–126.
- [3] S. Cui, H. Pu, S. A. Wells, Z. Wen, S. Mao, J. Chang, M. C. Hersam, J. Chen, *Nat. Commun.* **2015**, *6*, 8632.
- [4] K. Lee, H. Kim, M. Lotya, J. N. Coleman, G. Kim, G. S. Duesberg, *Adv. Mater.* **2011**, *23*, 4178–4182.
- [5] K. Chang, W. Chen, *ACS Nano* **2011**, *5*, 4720–4728.
- [6] J. Deng, H. Li, J. Xiao, Y. Tu, D. Deng, H. Yang, H. Tian, J. Li, P. Ren, X. Bao, *Energy Environ. Sci.* **2015**, *8*, 1594–1601.
- [7] K. S. Novoselov, A. K. Geim, S. V. Morozov, D. Jiang, Y. Zhang, S. V. Dubonos, I. V. Grigorieva, A. A. Firsov, *Science* **2004**, *306*, 666–669.
- [8] V. Nicolosi, M. Chhowalla, M. G. Kanatzidis, M. S. Strano, J. N. Coleman, *Science* **2013**, *340*, 1226419.
- [9] J. Zheng, H. Zhang, S. Dong, Y. Liu, C. Nai, H. Shin, H. Jeong, B. Liu, K. Loh, *Nat. Commun.* **2014**, *5*, 2995.
- [10] Y. Shi, H. Li, L. Li, *Chem. Soc. Rev.* **2015**, *44*, 2744–2756.
- [11] D. Yoo, M. Kim, S. Jeong, J. Han, J. Cheon, *J. Am. Chem. Soc.* **2014**, *136*, 14670–14673.
- [12] C. Wang, J. Li, X. Lv, Y. Zhang, G. Guo, *Energy Environ. Sci.* **2014**, *7*, 2831–2867.
- [13] E. Brillas, I. Sirés, M. A. Oturan, *Chem. Rev.* **2009**, *109*, 6570–6631.
- [14] A. Tiya-Djowe, S. Laminsi, G. L. Noupeyi, E. M. Gaigneaux, *Appl. Catal. B.* **2015**, *176*, 99–106.
- [15] J. Y. T. Chan, S. Ang, E. Ye, M. Sullivan, J. Zhang, M. Lin, *Phys. Chem. Chem. Phys.* **2015**, *17*, 25333–25341.
- [16] H. Chen, Z. Zhang, Z. Yang, Q. Yang, B. Li, Z. Bai, *Chem. Eng. J.* **2015**, *273*, 481–489.
- [17] B. Li, L. Chen, H. Zou, J. Lei, H. Luo, N. Li, *Nanoscale* **2014**, *6*, 9831–9838.
- [18] B. Qiu, M. Xing, J. Zhang, *J. Mater. Chem. A* **2015**, *3*, 12820–12827.
- [19] N. A. Zubir, C. Yacou, J. Motuzas, X. Zhang, X. S. Zhao, J. C. Diniz da Costa, *Chem. Commun.* **2015**, *51*, 9291–9293.
- [20] T. Zhu, W. L. Ong, L. Zhu, G. W. Ho, *Sci. Rep.* **2015**, *5*, 10601.
- [21] E. Neyens, J. Baeyens, *J. Hazard. Mater.* **2003**, *98*, 33–50.
- [22] J. Jeong, J. Yoon, *Water Res.* **2005**, *39*, 2893–2900.
- [23] M. Bykov, E. Bykova, S. van Smaalen, L. Dubrovinsky, C. McCammon, V. Prakapenka, H. P. Liermann, *Phys. Rev. B* **2013**, *88*, 014110.
- [24] I. Jarrige, Y. Cai, S. R. Shieh, H. Ishii, N. Hiraoka, S. Karna, W. Li, *Phys. Rev. B* **2010**, *82*, 165121.
- [25] M. G. Kanatzidis, C. Wu, H. O. Marcy, D. C. DeGroot, C. R. Kannewurf, A. Kostikas, V. Papaefthymiou, *Adv. Mater.* **1990**, *2*, 364–366.
- [26] X. Yang, P. Tian, X. Zhang, X. Yu, T. Wu, J. Xu, Y. Han, *AIChE J.* **2015**, *61*, 166–176.
- [27] X. Yang, X. Xu, J. Xu, Y. Han, *J. Am. Chem. Soc.* **2013**, *135*, 16058–16061.
- [28] N. A. North, C. Pearson, *Stud. Conserv.* **1977**, *22*, 146–157.
- [29] D. Voiry, H. Yamaguchi, J. Li, R. Silva, D. C. B. Alves, T. Fujita, M. Chen, T. Asefa, V. B. Shenoy, G. Eda, M. Chhowalla, *Nat. Mater.* **2013**, *12*, 850–855.
- [30] H. Li, J. Wu, Z. Yin, H. Zhang, *Acc. Chem. Res.* **2014**, *47*, 1067–1075.
- [31] N. I. Kovtyukhova, Y. Wang, A. Berkdemir, R. Cruz-Silva, M. Terrones, V. H. Crespi, T. E. Mallouk, *Nat. Chem.* **2014**, *6*, 957–963.
- [32] X. Li, X. Wu, J. Yang, *J. Am. Chem. Soc.* **2014**, *136*, 11065–11069.
- [33] B. Sachs, T. O. Wehling, K. S. Novoselov, A. I. Lichtenstein, M. I. Katsnelson, *Phys. Rev. B* **2013**, *88*, 201402.
- [34] S. Zhao, Z. Li, J. Yang, *J. Am. Chem. Soc.* **2014**, *136*, 13313–13318.
- [35] W. Wang, S. Dai, X. Li, J. Yang, D. J. Srolovitz, Q. Zheng, *Nat. Commun.* **2015**, *6*, 7853.
- [36] J. Shen, Y. He, J. Wu, C. Gao, K. Keyshar, X. Zhang, Y. Yang, M. Ye, R. Vajtai, J. Lou, P. M. Ajayan, *Nano Lett.* **2015**, *15*, 5449–5454.
- [37] C. J. Shih, M. S. Strano, D. Blankschtein, *Nat. Mater.* **2013**, *12*, 866–869.
- [38] Y. Henez, V. Nicolosi, M. Lotya, F. M. Blighe, Z. Sun, S. De, I. T. McGovern, B. Holland, M. Byrne, Y. K. Gun'ko, J. J. Boland, P. Niraj, G. Duesberg, S. Krishnamurthy, R. Goodhue, J. Hutchison, V. Scardaci, A. C. Ferrari, J. N. Coleman, *Nat. Nano.* **2008**, *3*, 563–568.
- [39] S. Jeong, D. Yoo, M. Ahn, P. Miró, T. Heine, J. Cheon, *Nat. Commun.* **2015**, *6*, 5763.
- [40] C. Wu, D. C. DeGroot, H. O. Marcy, J. L. Schindler, C. R. Kannewurf, T. Bakas, V. Papaefthymiou, W. Hirpo, J. P. Yesinowski, *J. Am. Chem. Soc.* **1995**, *117*, 9229–9242.
- [41] F. Song, X. Hu, *Nat. Commun.* **2014**, *5*, 4477.
- [42] X. Fan, P. Xu, D. Zhou, Y. Sun, Y. Li, M. A. T. Nguyen, M. Terrones, T. E. Mallouk, *Nano Lett.* **2015**, *15*, 5956–5960.
- [43] H. Liu, A. T. Neal, Z. Zhu, Z. Luo, X. Xu, D. Tománek, P. Ye, *ACS Nano* **2014**, *8*, 4033–4041.
- [44] J. R. Brent, D. J. Lewis, T. Lorenz, E. A. Lewis, N. Savjani, S. J. Haigh, G. Seifert, B. Derby, P. O'Brien, *J. Am. Chem. Soc.* **2015**, *137*, 12689–12696.
- [45] J. J. Pignatello, E. Oliveros, A. MacKay, *Crit. Rev. Environ. Sci. Technol.* **2006**, *36*, 1–84.
- [46] P. Nissenon, D. Dabdub, R. Das, V. Maurino, C. Minerio, D. Vione, *Atmos. Environ.* **2010**, *44*, 4859–4866.
- [47] H. Kusic, N. Koprivanac, A. L. Bozic, I. Selanec, *J. Hazard. Mater.* **2006**, *136*, 632–644.
- [48] M. Pimentel, N. Oturan, M. Dezotti, M. A. Oturan, *Appl. Catal. B* **2008**, *83*, 140–149.
- [49] J. A. Zazo, J. A. Casas, A. F. Mohedano, M. A. Gilarranz, J. J. Rodriguez, *Environ. Sci. Technol.* **2005**, *39*, 9295–9302.
- [50] T. T. Vu, G. Marbán, *Appl. Catal. B* **2014**, *152*, 51–58.
- [51] W. P. Kwan, B. M. Voelker, *Environ. Sci. Technol.* **2003**, *37*, 1150–1158.
- [52] K. Zhao, L. Zhang, J. Wang, Q. Li, W. He, J. Yin, *J. Am. Chem. Soc.* **2013**, *135*, 15750–15753.

- [53] J. Bao, X. Zhang, B. Fan, J. Zhang, M. Zhou, W. Yang, X. Hu, H. Wang, B. Pan, Y. Xie, *Angew. Chem. Int. Ed.* **2015**, *54*, 7399–7404; *Angew. Chem.* **2015**, *127*, 7507–7512.
- [54] S. Parra, L. Henao, E. Mielczarski, J. Mielczarski, P. Albers, E. Suvorova, J. Guindet, J. Kiwi, *Langmuir* **2004**, *20*, 5621–5629.
- [55] M. A. Voinov, J. O. S. Pagán, E. Morrison, T. I. Smirnova, A. I. Smirnov, *J. Am. Chem. Soc.* **2011**, *133*, 35–41.
- [56] J. Yu, Q. Xiang, M. Zhou, *Appl. Catal. B* **2009**, *90*, 595–602.
- [57] J. Yu, W. Wang, B. Cheng, B. Su, *J. Phys. Chem. C* **2009**, *113*, 6743–6750.
- [58] M. Zhou, J. Zhang, B. Cheng, H. Yu, *Int. J. Photoenergy* **2012**, 532843.
- [59] G. Kresse, J. Furthmüller, *Phys. Rev. B* **1996**, *54*, 11169–11186.
- [60] J. P. Perdew, A. Zunger, *Phys. Rev. B* **1981**, *23*, 5048–5079.
- [61] J. P. Perdew, J. A. Chevary, S. H. Vosko, K. A. Jackson, M. R. Pederson, D. J. Singh, C. Fiolhais, *Phys. Rev. B* **1992**, *46*, 6671–6687.
- [62] S. Grimme, *J. Comput. Chem.* **2006**, *27*, 1787–1799.
- [63] H. J. Monkhorst, J. Pack, *Phys. Rev. B* **1976**, *13*, 5188–5192.
- [64] S. R. Hwang, W.-H. Li, K. C. Lee, J. W. Lynn, C.-G. Wu, *Phys. Rev. B* **2000**, *62*, 14157–14163.
- [65] Z. Zhao, W. Dai, *Inorg. Chem.* **2014**, *53*, 13001–13011.
- [66] K. Otte, W. W. Schmahl, R. Pentcheva, *J. Phys. Chem. C* **2013**, *117*, 15571–15582.

Received: January 14, 2016

Published online on May 24, 2016